

## **Fe and S-isotope compositions of hydrothermal deposits from Kings Triple Junction, Lau Basin, southwest Pacific Ocean**

**Durbar Ray<sup>1</sup>, Bulusu Sreenivas<sup>2,\*</sup>, SuryaPrakash L.<sup>1,3</sup>, Aninda Mazumdar<sup>1</sup>,  
Aditya Peketi<sup>1</sup>, Anil L. Paropkari<sup>1</sup>, G. Balu<sup>2</sup>**

<sup>1</sup> CSIR-National Institute of Oceanography, Goa - 403004, India

<sup>2</sup> CSIR-National Geophysical Research Institute, Hyderabad - 500007, India

<sup>3</sup>Present address: National Centre for Polar and Ocean Research, Headland Sada,  
Vasco da Gama, Goa- 403804, India.

\*Corresponding author: Bulusu Sreenivas,  
CSIR-National Geophysical Research Institute,  
Hyderabad - 500007, India; Email: bsreenivas@ngri.res.in

### **Abstract**

We analyzed iron and sulfur isotope compositions of polymetallic sulfides from an extinct hydrothermal mound near the Kings Triple Junction of the northern Lau basin belonging to a back-arc basin for understanding the origin and mineral zoning processes in this study. Sulfides from the hydrothermal mound's pedestal slab consisting of chalcopyrite and pyrite show enrichment of heavy S-isotope ( $\delta^{34}\text{S}_{\text{V-CDT}} = +8.3$  to  $+9.6\%$ ). Sphalerite-dominated chimney on the mound's slope also has variable  $\delta^{34}\text{S}$  values between  $+5.5$  and  $+8.3\%$  from central orifice to outer wall. These isotopic ratios indicate the substantial contribution of heavy isotope rich sulfate-S in seawater circulating within the mound. Low  $\Delta^{33}\text{S}$  values in these sulfides also indicate that the sulfate reduction is of thermal origin, with minimal or no role for microbes. Circulating seawater induced changes in fluid composition and post-depositional zone refinement of certain minerals can explain the variation in  $\delta^{34}\text{S}$  in different layers within the chimney and pedestal slab. The Fe-isotope compositions ( $\delta^{56}\text{Fe}_{\text{IRMM-014}}$ ) show a range from  $-1.1$  to  $-0.3\%$  in the pedestal slab while they vary between  $-1.7$  and  $-0.6\%$  at different parts of the peripheral chimney section. We explain such changes are mostly due to redox processes and mineral zoning development during these sulfide deposit formation. The tree-like Fe-Mn oxide growth structures in the vicinity of the hydrothermal mound having a thin birnessite top layer and amorphous iron oxide bottom part show distinct  $\delta^{56}\text{Fe}$  values of  $-3.0$  and  $-0.8\%$ , respectively.

**Keywords:** Lau basin, hydrothermal sulfide, ferromanganese oxide, sulfur isotopes, iron isotopes.

## 1. Introduction

Hydrothermal vent systems play a critical role in maintaining seawater chemical composition. They act as chemical reactors in adding and removing certain elements and thus maintain ocean chemistry. Removal of elements such as Mg and S from seawater and the addition of Fe has significant influence; however, their critical role remains largely uncertain (Elderfield and Schulz, 1996). The average dissolved Fe content in seawater is in nM levels or lower (e.g. Conway et al., 2016), but the hydrothermal fluxes are considered an important contributor to its budget. In general, the hydrothermal Fe precipitates close to the hydrothermal field (German and Von Damm, 2003). Earlier hydrothermal Fe fluxes are estimated to be as low as 0.4 to 2.9 % of the total influx (Elderfield and Schultz, 1996). However, recent estimates suggest that the hydrothermal contribution in the total dissolved Fe may vary from 2 to 75% (Conway and John, 2014; Tagliabue et al., 2010; Saito et al., 2013; Carazzo et al., 2013; Dauphas et al., 2017). The initial clue suggesting the crucial role of hydrothermal Fe is the correlation between excess  $^3\text{He}$  and Fe concentration (Boyle et al., 2005). As hydrothermal fluids pass through the seafloor, they leach Fe from the surrounding rocks, yielding up to millimolar Fe concentrations, many orders of magnitude higher than deep ocean seawater. If all of this Fe remains dissolved in seawater, it would have a considerable impact on global ocean Fe concentrations (Dauphas et al., 2017). However, when hot and reducing hydrothermal fluids mix with the surrounding colder and more oxygenated seawater, nearly all hydrothermal Fe precipitates as oxyhydroxide minerals close to the hydrothermal vents (e.g., German and Seyfried, 2014). It was also suggested that a small portion of hydrothermal Fe could be stabilized within hydrothermal plumes through binding with dissolved and particular organic ligands (Bennett et al. 2008; Toner et al. 2009), and this hydrothermal Fe is transported to significant distances in the ocean (Toner et al., 2009; Wu et al., 2011; Saito et al., 2013; Resing et al., 2015; Fitzsimmons et al., 2014, 2017). Increased Fe concentrations due to hydrothermal activity are found hundreds and thousands of kilometers from the vents (Conway and John, 2014; Resing et al., 2015). Thus hydrothermal iron is an integral part of the surface ocean productivity, especially in Fe-limited high nutrient low chlorophyll Southern Ocean (Tagliabue et al., 2010; 2014). The Fe isotope record ( $\delta^{56}\text{Fe}\text{‰ IRMM-014} = [\{(^{56}\text{Fe}/^{54}\text{Fe}_{\text{sample}})/(^{56}\text{Fe}/^{54}\text{Fe}_{\text{IRMM-014}})\}-1]\times 1000$ ) of Fe-Mn crusts do reveal that such deep sourced hydrothermal Fe might have been influential in the geological past as well (cf. Chu et al., 2006; Horner et al., 2014). The Fe isotope compositions of hydrothermal iron are generally  $^{54}\text{Fe}$ -enriched, with  $\delta^{56}\text{Fe}$  values from  $-0.2$  to  $-0.3\text{‰}$  (Beard et al. 2003; Rouxel et al. 2004, 2008, 2016; Severmann et al. 2004; Sharma et al. 2001). The buoyant plume particles dominated by oxyhydroxides are enriched in heavier Fe isotopes (Severmann et al., 2004), while the

sulfide particles with lighter ones (Bennett et al., 2009; Rouxel et al., 2016). Conway and John (2014) have shown evidence from the Trans-Atlantic Geotraverse (TAG) vent site that the hydrothermal plume particles not in the immediate vicinity also are characterized by  $^{54}\text{Fe}$  enrichment. Most of the Fe isotope studies on hydrothermal vent fluids or deposits are from the - mid-ocean ridge settings. Therefore, it is vital to characterize isotope compositions of hydrothermal deposits from various geological settings such as back-arc basins to assess the complete spectrum of the associated processes and understand the more extensive influence on marine chemistry.

The subduction of the western part of the Pacific plate has led to the development of several active arc-trench systems and marginal basins (e.g., Lau, Fiji, Woodlark, Manus basins, Mariana, Soufugan, Izu-Bonin, Okinawa troughs, etc.), which are well known for hydrothermal mineral deposits (Fouquet et al., 1991; Lisitsyn et al., 1992; 1993; Glasby and Natsu, 2003; Paropkari et al., 2010; Sun et al., 2012). Earlier, several studies have addressed these hydrothermal deposits' formation mechanisms, mostly based on mineralogy and elemental geochemistry (Lisitsyn et al., 1992; Humphris et al., 1995; Paropkari et al., 2010; Ray et al., 2014; 2018). However, to know the evolutionary history of any hydrothermal deposit, it is essential to understand processes involved in the fluid generation and mineral precipitation (Janecky and Shanks, 1988; Tivey et al., 1995; Rouxel et al., 2008). Recent studies have shown that the isotopic compositions of hydrothermal deposits are useful proxies of geochemical reactions responsible for the evolution of these deposits (Johnson et al., 2004; Rouxel et al., 2004; 2008, Zeng et al., 2017; Li et al., 2018). Notably, the stable isotopic ratios of commonly available elements like S and Fe in hydrothermal deposits could provide information about the nature of source materials and reaction conditions prevailing during the genesis of these deposits (Rouxel et al., 2004, 2008). As infiltrated seawater and basement rock are the primary sources of S for generating hydrogen sulfide in hydrothermal fluids, the S-isotopic compositions of sulfide minerals are useful in tracing the water-rock interactions involved in subsurface reactions (Shanks, 2001). Similarly, the temperature, pH, Eh, and chemical composition of fluids control hydrothermal Fe precipitation (Severmann et al., 2004). Thus the Fe-isotope ratios in hydrothermal deposits could reflect those conditions. Despite several geochemical studies on hydrothermal deposits from the marginal basins in the western Pacific, such deposits' evolution based on isotope signatures is poorly constrained. The effects of entrained seawater on the melting of the subducting plate resulting in hydrated melts and their involvement in hydrothermal processes and subsequent deposits are rarely addressed, particularly in back-arc settings. In this study, we analyzed Fe and S-isotopic compositions in different mineral zones of three hydrothermal structures from an extinct hydrothermal mound near the Kings Triple Junction (KTJ), the northern Lau Basin. The

compositions of source fluid and the possible mode of formations of these hydrothermal deposits are inferred in the light of these isotope compositions.

## **2. Geological settings of Kings Triple Junction and its surroundings in the Lau basin**

Lau Basin is one of the marginal basins in the southwest Pacific Ocean separating the Tonga arc-trench system from the Lau ridge. The tectonic setting of this back-arc basin is defined by the Pacific plate's subduction under the Indo-Australian plate towards the east. The northern part of this basin is characterized by very high subduction rates of 120-145mm/yr (Hawkins, 1995). In the northeastern part of this basin, three spreading axes meet at Kings Triple Junction (KTJ) (15°30'S, 174°50'W), which is also known as Mangatolu Triple Junction (MTJ). Earlier investigation showed that the KTJ and the northern Lau back-arc basin have a complex geophysical setting where spreading centers overlap on each other and develop typical ridge-ridge-ridge type triple junction (Fig. 1, Hawkins, 1995). Parsons and Tiffin (1993) described the KTJ as an intensely deformed neovolcanic area. The axial ridges have narrow rift valleys, and from the KTJ, three valleys deepen towards the south, southeast, and northeast (Fig. 1, Lisitsyn et al., 1992). The average seafloor depth of the area around KTJ is between 1800 and 2500m. Rocks from KTJ and nearby areas are mostly basaltic to basaltic-andesite type (Dril et al., 1997). Typical andesitic lava was sampled from the base of the sulfide mound (Falloon et al., 1992). Detailed descriptions of the hydrothermal field at KTJ and its different structures are described by Paropkari et al (2010).

## **3. Sampling and sample description**

During the 19<sup>th</sup> cruise of *RV Akademik Mstislav Keldysh* in 1990, the hydrothermal field near KTJ was explored thoroughly with the MIR submersible. At the water depth of 2050 m, a large extinct field of an approximate dimension of 2 km in length and 200 m in width on the northwest segment of KTJ (15°23.2'S, 174°40.1'W, Fig. 1, Lisitsyn et al., 1992) was photographed and sampled. A schematic of the extinct hydrothermal field and sampled regions are shown in Fig. 2a. Mostly, polymetallic sulfides and oxides were sampled from that field during the MIR dive (M2226). For the present study, three types of hydrothermal deposits, viz., peripheral chimney, pedestal slab, and ferromanganese oxides (Fig. 2c to e) from that extinct field, have been selected.

The first sample, M2226-5, is a Cu and Fe-rich sulfide from a vertical section of the pedestal slab, representing the hydrothermal mound's main basement. Sub-sampling of this section for isotopic analyses was made based on small scale mineral zonings shown in Fig. 2d. Among four layers (L1 to L4, Fig. 2d) of this section, L1 represents a deeper layer, while porous L4 corresponds to the surface layer. All the pedestal slab layers mostly contain chalcopyrite and pyrite (Figs. 3a and b). However,

the dark-colored L3 layer is dominated by sphalerite (Figs. 3c and d) and, therefore, differs from the other three layers geochemically (Paropkari et al., 2010).

The second sulfide sample, M2226-6, was obtained from a 0.7m tall hydrothermal chimney on the mound's slope. A 2cm thick horizontal section of this Zn-rich chimney (Fig. 2b) was used in this study. Six sub-samples (S1 to S6, Fig. 2c) with a width of ~1.5 cm each from the outer rim to the inner orifice were collected across this chimney section. Mineralogical analyses of individual sub-samples show that all of them are mostly composed of sphalerite (Table 1) with traces of pyrite and chalcopyrite (Paropkari et al., 2010). Secondary Electron Microscope images also reveal massive sphalerite with some patches of amorphous silica growths within these sections (Figs. 4a and 4c). Based on mineral assemblage and elemental compositions, a previous investigation indicated this light brown chimney section represents a low-temperature white smoker (Paropkari et al., 2010).

Several small tree-like ferromanganese oxide growths within the pillow basalts surround the hydrothermal mound (Fig. 2). This area is referred to as the "Christmas Tree" field (Lisitsyn et al., 1992). The Fe-Mn-oxide sample, M2226-12 (Fig. 2e), was obtained from a small oxide growth. In the two-layered structure of this oxide deposit, about 2-3cm thick top black coating (B-12; Fig. 2e) mostly contains birnessite (7Å manganate), while the orange-colored lower layer (O-12; Fig. 2e) contained amorphous Fe-Si-oxyhydroxide (Paropkari et al., 2010). Secondary Electron Microscope observations revealed that the B-12 layer comprises tiny globular or rosette-like particles (Fig. 5), similar to typical hydrothermal Mn-oxide deposits described at the Valu Fa Ridge of the southern Lau basin (Sun et al., 2012). The O-12 sample consisted of porous and fragile material (Fig. 5). Samples from both layers were analyzed for Fe-isotope compositions.

## **4. Analytical methods**

### ***4.1. Analysis of Fe isotopic composition***

Iron isotopic compositions were measured using a Multi-Collector-ICPMS (Nu plasma-HR) at CSIR-National Geophysical Research Institute, Hyderabad, India. In this method, 20 mg of dry powdered samples and reference standards were digested with an ultrapure acid mixture (HF:HNO<sub>3</sub>:HClO<sub>4</sub>: 7:3:1) and ultra sonicated. The Fe fractions from the digested aliquots were purified using 10ml of 2N HCl and 0.001% H<sub>2</sub>O<sub>2</sub> mixture and AG-MP1 anion exchange resin (Marèchal et al., 1999). The recovery of Fe was more than 97% based on the estimations on reference standards BCR-2 and IF-G using Atomic Absorption Spectroscopy. The eluted fractions were evaporated and re-dissolved in 2% ultra-pure HNO<sub>3</sub>. All the chemical procedures are carried out in clean laboratory facilities equipped with class 100 laminar flow hoods. The Fe isotopic

analysis was carried out on a Nu HR MC-ICP-MS using pseudo-high-resolution mode with a resolution of about 5000. Standard-Sample-Bracketing (SSB) method was employed (Albarede and Beard, 2004) using IRMM-014 as the standard reference material. The long term precision on IRMM-014 is  $\pm 0.04\%$  ( $1\sigma$ ,  $n = 71$ ). Both sample and standard solutions were analyzed repeatedly ( $n = 3$  to  $5$ ), and the average, standard deviation values ( $1\sigma$ ) of these replicate analyses are reported. The Fe isotope results are reported as  $\delta^{56}\text{Fe}$  (‰) relative to standard IRMM-014 as  $\delta^{56}\text{Fe}_{\text{IRMM-014}} = [\{(^{56}\text{Fe}/^{54}\text{Fe}_{\text{sample}})/(^{56}\text{Fe}/^{54}\text{Fe}_{\text{IRMM-014}})\} - 1] \times 1000$ . The geological standards BCR-2 and IF-G analyzed along with samples yielded  $\delta^{56}\text{Fe}$  values of  $0.04 \pm 0.06\%$  ( $1\sigma$ ,  $n=5$ ) and  $0.71 \pm 0.07\%$  ( $1\sigma$ ,  $n=5$ ) against the reported values of  $0.039 \pm 0.03\%$  ( $1\sigma$ ) and  $0.63 \pm 0.10\%$  ( $1\sigma$ ), respectively (Dauphas and Rouxel, 2006).

#### 4.2. Analysis of S isotopic composition

Bulk S-isotope ratios of all samples were determined using a Thermo Delta V plus IRMS coupled with an elemental analyzer (EA1112) in continuous flow mode at CSIR-National Institute of Oceanography, Goa. A mixture of homogenized sulfide sub-sample and  $\text{V}_2\text{O}_5$  in a tin capsule was completely combusted at  $1150^\circ\text{C}$  to produce  $\text{SO}_2$ . Water vapor produced during combustion was trapped by using a moisture trap. The  $\text{SO}_2$  was separated from other gases such as  $\text{N}_2$  and  $\text{CO}_2$  on a packed GC column at a temperature of  $60^\circ\text{C}$ . The stable isotopic compositions are reported with conventional delta notation, standardized to Vienna-Canyon Diablo Troilite (V-CDT) standard (Coplen and Krouse, 1998) as  $\delta^{34}\text{S}_{\text{V-CDT}} = [\{(^{34}\text{S}/^{32}\text{S}_{\text{sample}})/(^{34}\text{S}/^{32}\text{S}_{\text{V-CDT}})\} - 1] \times 1000$ . IAEA standards SO-5 ( $\text{BaSO}_4$ :  $+0.5\%$  V-CDT), SO-6 ( $\text{BaSO}_4$ :  $-34.1\%$  V-CDT), NBS127 ( $\text{BaSO}_4$ :  $+22.3\%$  V-CDT), S-1 ( $\text{Ag}_2\text{S}$ :  $-0.3\%$  V-CDT) and S-2 ( $\text{Ag}_2\text{S}$ :  $+22.7\%$  V-CDT) were used for the preparation of calibration curves. The reproducibility ( $1\sigma$ ) as determined through replicate measurements is better than  $\pm 0.3\%$ , and the accuracy is well within the precision limits.

Two representative samples from pedestal slab and chimney (i.e., L3 and S6 respectively) have also been analyzed for multiple S-isotopes ( $^{32}\text{S}$ ,  $^{33}\text{S}$ ,  $^{34}\text{S}$ , and  $^{36}\text{S}$ ) at the Stable Isotope Laboratory of McGill University. Sulfur in sulfide samples was converted to  $\text{Ag}_2\text{S}$  through a Cr(II) reduction procedure following Canfield et al. (1986). The extracted  $\text{Ag}_2\text{S}$  was then fluorinated at  $225^\circ\text{C}$  in a Ni bomb under  $\sim 20\times$  stoichiometric excess of  $\text{F}_2$  for  $>9.0$  hrs to produce  $\text{SF}_6$ , which was then purified cryogenically and chromatographically and analyzed on a Thermo Electron MAT 253 Mass spectrometer for multiple sulfur isotope ratios in a dual-inlet mode. S-isotope compositions ( $\delta^{33}\text{S}$ ,  $\delta^{34}\text{S}$ ,  $\delta^{36}\text{S}$ ,  $\Delta^{33}\text{S} = \delta^{33}\text{S} - 1000(1 + \delta^{34}\text{S}/1000)^{0.515} - 1$  and  $\Delta^{36}\text{S} = \delta^{36}\text{S} - 1000(1 + \delta^{34}\text{S}/1000)^{1.91} - 1$ ) are reported with reference to V-CDT and reported in Table 1. The results were measured against

international standard reference material IAEA-S-1 ( $\delta^{34}\text{S}=-0.3\text{‰}$  and  $\Delta^{33}\text{S}=-0.061\text{‰}$ ) and estimated analytical maximum errors estimated by repeated measurement of standards for  $\delta^{34}\text{S}$ ,  $\Delta^{33}\text{S}$  and  $\Delta^{36}\text{S}$  are 0.2‰, 0.02‰ and 0.2‰, respectively.

## 5. Results

### 5.1. S and Fe isotope compositions in pedestal slab

The Cu and Fe-rich sulfides from the pedestal slab are characterized with heavier S-isotope ( $\delta^{34}\text{S}=+8.3$  to  $+9.5\text{‰}$  VCDT) and lighter Fe-isotopic compositions ( $\delta^{56}\text{Fe}=-0.33\pm 0.02$  to  $-1.14\pm 0.05\text{‰}$  IRMM-014, Table 1). Distribution of S-isotope composition shows lower values ( $\delta^{34}\text{S}\leq 8.5\text{‰}$ ) in top layers (L3 and L4) as compared to the deeper layers ( $\delta^{34}\text{S}>+9.5\text{‰}$  in L1 and L2). The sphalerite dominated dark layer L3 has the most  $^{34}\text{S}$  depleted value ( $\delta^{34}\text{S}=8.3\text{‰}$ ) with a  $\Delta^{33}\text{S}$  value of  $-0.014\pm 0.007\text{‰}$ . The layers L1, L2, and L4 are rich in bulk iron contents (Fe wt. % =8.1 to 12.5%, Table 1) and show a close range of Fe-isotopic ratios ( $\delta^{56}\text{Fe}=-0.96$  to  $-1.14\text{‰}$ , Table 1). Sample L3 is relatively depleted in Fe (2.9wt. %) but has a distinctly enriched  $\delta^{56}\text{Fe}$  value of  $-0.33\pm 0.02\text{‰}$  (Table 1) compared to all the layers.

### 5.2. S and Fe isotope compositions in the peripheral chimney

Similar to the pedestal slab, the sphalerite-dominated peripheral chimney samples showed  $\delta^{34}\text{S}$  values ranging between  $+5.5$  and  $+8.3\text{‰}$ ; while the  $\delta^{56}\text{Fe}$  ranged between  $-0.62\pm 0.05$  and  $-1.70\pm 0.01\text{‰}$ . Variations of both Fe and S-isotopic ratios are large from the outer rim (S1) to inner orifice sections (S5 or S6) across the chimney-wall. The  $\delta^{34}\text{S}$  values show a gradual increase from outer rim ( $+5.5\text{‰}$  in S1) towards orifice ( $+8.1$  and  $+8.3\text{‰}$  in S5 and S6 respectively), significantly higher than the analytical precision of  $\pm 0.3\text{‰}$  (Table 1). The sulfide from layer S6 has a  $\Delta^{33}\text{S}$  value of  $0.009\text{‰}$ . The distribution of Fe-isotope composition did not show any specific trend across this chimney wall. Among the chimney sections, S6 encircling the fluid orifice showed maximum enrichment of lighter Fe isotopes ( $\delta^{56}\text{Fe}=-1.70\pm 0.01\text{‰}$ ); while the outermost section, S1 showed heavier isotopic composition ( $\delta^{56}\text{Fe}=-0.62\pm 0.04\text{‰}$ ) (Table 1).

### 5.3. Fe isotope composition in ferromanganese-oxide growths within pillow basalts

Analyses of Fe isotopes in the samples from O-12 and B-12 layers of ferromanganese oxide growth showed isotopically lighter compositions. The orange-colored Fe-rich (bulk Fe =14.5wt. %) ochre, O-12 from the lower part of the oxide growths had  $\delta^{56}\text{Fe}$  value  $-0.81\pm 0.02\text{‰}$ . However, the black manganese-rich (bulk Mn =32.2wt.%) surface layer, B-12, showed the lowest  $\delta^{56}\text{Fe}$  value of  $-3.0\pm 0.10\text{‰}$  (Table 1).

## 6. Discussion

### 6.1. S and Fe isotope compositions in pedestal slab: Evidence for zone refinement

The  $\delta^{34}\text{S}$  values of all four layers of pedestal slab, M2226-5, ( $\delta^{34}\text{S} = +8.3$  to  $+9.8\%$ ) are lying within the range ( $\delta^{34}\text{S} = -2.0$  to  $+11\%$ ) of hydrothermal sulfides deposited in back-arc systems (Gemmell et al., 1996; Herzig et al., 1998); but are heavier than most of the sulfides from sediment-free mid-oceanic ridges ( $\delta^{34}\text{S} = -0.8$  to  $+6.2\%$ , e.g., Styrer et al., 1981; Shanks and Seyfried, 1987; Woodruff and Shanks, 1988; Bluth and Ohmoto, 1988; Duckworth et al., 1995; Herzig et al., 1998; Rouxel et al., 2004; Zeng et al., 2017). Different sources and precipitation mechanisms of hydrothermal fluid have been proposed to explain the variations of  $\delta^{34}\text{S}$  values in sulfides (e.g., Woodruff and Shanks, 1988; Janecky and Shanks, 1988; Shanks, 2001; Ono et al., 2007; Rouxel et al., 2008). In hydrothermal deposits, sulfur is usually contributed from two primary sources: (i) leaching of igneous rocks and (ii) reduction of seawater-sulfate. The reduced sulfur originating from very high-temperature hydrothermal reactions has isotopic ratios,  $\delta^{34}\text{S} < +5.0\%$  (Styrer et al., 1981). However, a further increase in  $\delta^{34}\text{S}$  values could result from the subsurface reduction of seawater sulfate ( $\delta^{34}\text{S}_{\text{sulfate}} = +21\%$ , Rees et al., 1978) or dissolution of anhydrite in the up-flow zone of hydrothermal mounds. Chiba et al. (1998) interpreted higher  $\delta^{34}\text{S}$  values of  $+6.6$  to  $+8.8\%$  in sulfides from the Trans-Atlantic Geotraverse (TAG) hydrothermal mound as a result of reduction of aqueous sulfate and anhydrite in the reaction zone. It appears that a similar isotopic fractionation mechanism influenced by percolating seawater is responsible for the isotope compositions of the KTJ sulfides. The coexistence of barite with sulfide minerals in layers L1 and L2 (Paropkari et al., 2010) also substantiates the contribution of seawater in hydrothermal mineralization of sulfides. Besides direct percolation of seawater, the subduction of hydrated crust and sediments also carries seawater components and thus contribute heavy S-isotope in magmatic melts, particularly in back-arc settings.

In the pedestal slab of the KTJ mound, the sulfides in deeper layers (L1 and L2) are characterized by higher  $\delta^{34}\text{S}$  values ( $> +9.6\%$ ) as compared to shallow layers (L3 and L4) ( $\delta^{34}\text{S} < +8.5\%$ ). Such S-isotope variations could originate from sub-surface reactions between pre-existing sulfate or sulfide deposits and re-circulating fluid (Janecky and Shanks, 1988). In the KTJ mound, Paropkari et al. (2010) proposed that the subsurface zone refinement mechanisms mediated by percolated seawater are responsible for the mineral and trace element distributions in the pedestal slab. By these mechanisms, seawater circulating within the mound causes rapid precipitation of chalcopyrite and pyrite in deeper layers and generates acidic fluid, which dissolves and remobilize certain elements (e.g., Zn) towards the near-surface zone (Tivey et al., 1995; Wagner and Cook, 1998; Paropkari et al., 2010). Such remobilization process probably carries lighter S-isotopes to the fluid phase, which



likely ascends upward along with dissolved Zn, which is reflected in the moderate negative correlation between bulk Zn concentrations and  $\delta^{34}\text{S}$  values ( $R^2 = 0.63$ ) in these layers of the pedestal slab (Fig. 6a). We propose that the sphalerite layer- L3 represents the precipitation front of Zn-sulfide developed during zone refinement. The lower  $\delta^{34}\text{S}$  values (+8.3‰) and relative increase of Zn concentration in L3, compared to deeper layers (Table 1), confirm the fractionation mechanism mediated by seawater circulating within the mound.

The Fe-isotope compositions in the four layers of the pedestal slab also show a considerable variation ( $\delta^{56}\text{Fe} = -0.33\text{‰}$  to  $-1.14\text{‰}$ ; Table 1) but lie within the range found in hydrothermal sulfides from 9-10°N EPR ( $\delta^{56}\text{Fe} = -0.06$  to  $-1.89\text{‰}$ ; Rouxel et al., 2008), JdFR, and MAR ( $\delta^{56}\text{Fe} = -0.3$  to  $-1.4\text{‰}$ ; Sharma et al., 2001). These estimated ratios show that the pyrite and chalcopyrite rich layers of the pedestal slab (i.e., L1, L2, and L4) have significant lighter compositions ( $\delta^{56}\text{Fe} = -0.96$  to  $-1.14\text{‰}$ ); while the sphalerite dominated layer, L3, has distinctly different Fe-isotopic ratio with heavier isotope enrichment ( $\delta^{56}\text{Fe} = -0.33\text{‰}$ ). Earlier studies showed that the high temperature ( $>300^\circ\text{C}$ ) sulfides like chalcopyrite (a dominant mineral in the pedestal slab) are characterized by limited Fe-isotope fractionation usually due to rapid establishment of isotopic equilibrium between  $\text{Fe(II)}_{\text{aq}}$ ,  $\text{FeS}_{\text{aq}}$ , and  $\text{CuFeS}_2$  (Rouxel et al., 2008 and references therein). Thus the average Fe-isotopic composition of hydrothermal chalcopyrite mostly lies within the limit of  $\delta^{56}\text{Fe}_{\text{chalcopyrite}} = 0.12 \pm 0.24\text{‰}$  (Li et al., 2018). Therefore, compared to this average ratio of chalcopyrite, the lighter Fe-isotope compositions of sulfides in L1, L2, and L4 layers cannot be explained based only on chalcopyrite precipitation mechanism, and the contribution from the coexisting pyrite should also be considered. Experiments with synthetic and natural pyrite samples showed that the ligand exchange between dissolved Hexa-aqua Fe(II) complexes and Fe-sulfides generates isotopically lighter hydrothermal iron-sulfides (Butler et al., 2005; Rouxel et al., 2008; Bennett et al., 2009; Guilbaud et al., 2011). Hence, the observed lighter Fe-isotope compositions in the layers L1, L2, L4 might be due to the dominant impact of rapid precipitation kinetics of iron sulfide (pyrite) from dissolved  $\text{Fe(II)}_{\text{aq}}$  in the hydrothermal fluid. It is expected that the Fe sulfide precipitation is not very fast in subsurface reaction zones; however, in back-arc settings, enhanced precipitation kinetics are possible mainly due to the cooling effect of the entrained seawater. The correlation between  $\delta^{56}\text{Fe}$  values and Fe concentrations ( $R^2 = 0.77$ , Fig. 6c) in the pedestal slab samples suggests that the pyrite formation kinetics are responsible for the observed  $\delta^{56}\text{Fe}$  values. A weak correlation between  $\delta^{56}\text{Fe}$  and Cu ( $R^2 = 0.45$ , Fig. 6d) in these samples points to the effect of equilibrium fractionation associated with chalcopyrite precipitation. Significant depletion of lighter Fe-isotopes in the Fe-poor L3 layer could be due to the absence of primary Fe-bearing sulfides.

The distribution of Fe-isotopic compositions showed a systematic decrease in  $\delta^{56}\text{Fe}$  values from the layers L3 to L1 (Table 1). Post-depositional zone refinement, a typical process mediated by seawater entrained within the hydrothermal mound, causes conductive cooling in the deep subsurface zones (Paropkari et al., 2010). This process allows relatively fast precipitation of Fe-sulfides and, therefore, enrichment of  $^{54}\text{Fe}$  in sulfide phases. This kinetic effect is expected to become less prominent as the temperature of circulating seawater increases during its upwards percolation. Besides this temperature effect, the redox changes also affect Fe isotope fractionation. A recent study indicates that abiotic redox changes affect the hydrothermal mixing processes (McDermott et al., 2020). The transfer of Fe from ferrous to ferric under biological and abiological conditions induces a fractionation of +1.5 to 3.2‰ (Croal et al., 2004, Swanner et al., 2017; Welsch et al., 2003). The Ce anomalies are important proxies for paleo redox conditions because Ce(IV) is insoluble compared to Ce(III) and adsorbed onto the Fe and Mn hydroxides leading to Ce-depletion (German and Elderfield, 1990). The correlations between  $\delta^{56}\text{Fe}$ ,  $\delta^{34}\text{S}$ , and Ce anomalies of the bulk samples (Figs. 7a and 7b) suggest that the kinetics of Fe-sulfide re-mineralization varied with the reducing nature of the fluid at different depth zones. These correlations are more pronounced for the samples of the pedestal slab than in the peripheral chimney. The ascending circulating seawater is expected to become more oxidized, resulting in higher Ce anomalies and reduced fractionation between Fe-dissolved and Fe-precipitated. Therefore, possibly the higher concentrations of dissolved sulfides/bisulfides at a deeper subsurface environment are also expected to enhance the precipitation kinetics of Fe-sulfides. The influence of seawater-mediated re-mineralization will be quantitatively more in the deeper part of the mound and gradually decrease towards the upper levels. The L3 layer has the maximum sphalerite content with minimal Fe (2.8 wt. %), indicating re-mineralization is extensive. The  $\delta^{56}\text{Fe} = -0.33 \pm 0.02$  ‰ of this sample suggests that the effect of kinetic isotope fractionation is least in the L3 layer. The  $^{54}\text{Fe}$  enrichment in the L4 ( $\delta^{56}\text{Fe} = -1.68 \pm 0.18$  ‰) layer probably points that the seawater induced post-depositional mineral zone refinement did not extend up to the surface layer of the hydrothermal mound or could be an indication of seawater alteration. We suggest that the subsurface process that controls the Fe-isotopic compositions of the pedestal slab sulfides is similar to the zone refinement mechanism described above for S-isotope distribution.

## ***6.2. S and Fe-isotope compositions in the peripheral chimney***

All six sub-samples of the chimney section (M2226-6/12) are enriched with  $^{34}\text{S}$ -isotope ( $\delta^{34}\text{S} = +5.5$  to  $+8.3$ ‰, Table 1) as compared to high-temperature hydrothermal sulfides from mid-oceanic ridges ( $\delta^{34}\text{S} < 5$ ‰, Styr et al., 1981; Rouxel et al., 2004) but, are similar to those reported in the Vailili hydrothermal field in the Lau basin ( $\delta^{34}\text{S} > +7.2$ ‰, Herzig et al., 1998) and the TAG

hydrothermal field (Chiba et al., 1998). Enrichment of  $^{34}\text{S}$  in these peripheral chimney samples suggests that the source fluid experienced subduction induced aqueous magmatic inputs with sulfate contribution from the seawater as proposed for the pedestal slab of the mound.

The distribution of S-isotope across the chimney section shows a gradual increase of  $\delta^{34}\text{S}$  values from the outer rim, S1 ( $\delta^{34}\text{S} = +5.5\%$ ) to the inner orifice, S6 ( $\delta^{34}\text{S} = +8.3\%$ , Table 1). Several studies have shown considerable S-isotopic variations within individual hydrothermal structures and were interpreted in terms of changes in fluid composition and mineral precipitation mode (Shanks, 2001; Rouxel et al., 2008). However, uniform mineral and elemental compositions in these chimney subsections (Table 1) suggest no significant fluid composition change during their growth. Therefore, mechanisms involved in mineral formation at different growth phases might be responsible for the observed  $\delta^{34}\text{S}$  variations across the chimney wall. During the initial growth phase, the porous chimney wall remains cooler compared to the later consolidated walls that retain temperature (Paropkari et al., 2010). Thus, in the chimney's inner part, the sulfide precipitation under warmer conditions might favor more S-isotopic equilibrium between sulfide minerals and sulfate in the hydrated fluid. Such equilibrium conditions may lead to  $^{34}\text{S}$  enrichment in inner chimney wall minerals.

The Fe-isotopic compositions of peripheral chimney sections are dominated with lighter values ( $\delta^{56}\text{Fe} = -0.62\%$  to  $-1.70\%$ , Table 1). Massive sulfides of active vent sites are characterized by lighter  $\delta^{56}\text{Fe}$  values (Rouxel et al., 2004; 2008). The pyrite and marcasite generally have the lowest  $\delta^{56}\text{Fe}$  values, while the chalcopyrite close to  $0\%$ . Such light Fe-isotopic compositions are thought to indicate kinetic isotope fractionation during sulfide precipitation because the precipitation of pyrite under equilibrium conditions would result in  $^{56}\text{Fe}$ -enrichment. The experimental (Syverson et al., 2013), observational (Polyakov et al., 2007; Polyakov and Sultanov, 2011), and theoretical (Blanchard et al., 2009) all point out such  $^{56}\text{Fe}$ -enrichment under equilibrium conditions. The  $\delta^{56}\text{Fe}$  values of the sphalerite chimney samples are lighter than high-temperature Cu-rich sulfides in black smokers (avg.  $\delta^{56}\text{Fe}_{\text{chalcopyrite}} = -0.12 \pm 0.24\%$ , Li et al., 2018) but comparable to Zn-rich hydrothermal sulfides ( $\delta^{56}\text{Fe} = -0.31$  to  $-2.00\%$ , Rouxel et al., 2008; Li et al., 2018), perhaps due to kinetic isotope fractionation. In our study, the  $\delta^{56}\text{Fe}$  values show a good correlation with Zn concentrations in these chimney sections (Fig. 6b), but they do not relate to Cu or Fe (Figs. 6c and 6d). Compared to the formation of Cu and Fe-rich hydrothermal sulfides, mineralization of sphalerite occurs under low-temperature conditions. Thus, the kinetically controlled Fe-isotope exchange is primarily responsible for the lighter Fe-isotope enrichment in Zn-rich chimney sulfides (Rouxel et al., 2008). Paropkari et al. (2010) suggested this chimney on the KTJ mound slope is similar to lower temperature white-

smoker based on mineralogy, elemental geochemistry, and physical features. Therefore, rapid sulfide precipitation from low-temperature fluids could have possibly caused the kinetic isotopic fractionation with preferable enrichment of lighter Fe-isotope in the chimney.

The  $\delta^{56}\text{Fe}$  values across the chimney wall samples show maximum enrichment of  $^{56}\text{Fe}$  isotopes ( $\delta^{56}\text{Fe} = -0.62\text{‰}$ ) at the outermost rim (S1) and gradually decreased in the intermediate sections (S2 – S5,  $\delta^{56}\text{Fe} = -0.97$  to  $-1.38\text{‰}$ ) and have the lowest value ( $\delta^{56}\text{Fe} = -1.70\text{‰}$ ) for the innermost orifice section (S6, Table 1). Despite comparable mineralogical composition, the observed variation of Fe-isotopic composition in all these chimney section samples is significant. Like S-isotope compositions, this variation in Fe-isotopic compositions could also result from changes in reaction kinetics during chimney development. The higher  $\delta^{56}\text{Fe}$  value for the outermost rim sample of the chimney (section S1), which predominantly comprises fine-grained sulfides and amorphous silica, could result from instantaneous precipitation of sulfides during the initial phase of chimney growth. The high  $\delta^{56}\text{Fe}$  value for sample S1 ( $\delta^{56}\text{Fe} = -0.62\text{‰}$ ) being similar to the average range of Fe-isotope ratios reported for typical hydrothermal fluids ( $\delta^{56}\text{Fe} = -0.59 \pm 0.39\text{‰}$ , Li et al., 2018) indicates equilibrium Fe isotopic exchange between the source fluid and sulfide phase. However, the low  $\delta^{56}\text{Fe}$  values of the inner wall samples (S2–S6,  $\delta^{56}\text{Fe} = -0.97$  to  $-1.70\text{‰}$ ) may indicate thermodynamically controlled fractionation, a result of precipitation of  $^{56}\text{Fe}$ -enriched sulfides in the initial phases leaving the fluid enriched in lighter Fe isotopes. The scattered correlations among  $\delta^{56}\text{Fe}$  and Fe, Cu, Zn (Fig. 7 b,c,d) coupled with low  $\delta^{56}\text{Fe}$  values may indicate that the isotopic exchange may be through kinetic fractionation. Thus, kinetically controlled processes might be responsible for enhanced isotopic fractionation with preferential enrichment of lighter Fe-isotopes in inner chimney section sulfides

### ***6.3 Implications of multiple S isotope compositions of sulfides***

Multiple S-isotope compositions of hydrothermal sulfides from the East Pacific Rise and the Mid-Atlantic Ridge gave evidence for an interplay among seawater, oceanic crust, microbial activity during hydrothermal activity (Ono et al., 2007). The two samples (L3 and S6) analyzed in this study for multiple S-isotopes yielded  $\Delta^{33}\text{S}$  values of  $0.014 \pm 0.007$  and  $0.009 \pm 0.004\text{‰}$ , respectively. These values are substantially lower than typical biogenic sulfides ( $\Delta^{33}\text{S} = 0.05$  to  $0.34\text{‰}$ , Ono et al., 2006) but resemble more the sulfides of thermogenic origin ( $\Delta^{33}\text{S} < 0.045\text{‰}$ , Ono et al., 2007). These results suggest that the role of microbial sulfate reduction is absent in these Lau Basin sulfides of back-arc settings.

#### 6.4. Fe-isotopic compositions in the ferromanganese oxide growth: Constraints on possible development

The sample M2226-12 represents the ferromanganese oxide growths on the seafloor around the KTJ mound. A previous study on mineralogy and geochemistry of this oxide indicates that they are formed by the precipitation of low temperature diffused fluid flow emanated through fractures within the pillows (Paropkari et al., 2010). Notably, low trace metal concentrations (e.g., Cu ~100 ppm, Ni <88ppm, Co <4.0ppm;  $\sum$ REE <1.9ppm), negative Ce, and positive Eu-anomalies (Table 1) of these oxide samples are similar to typical hydrothermal ferromanganese oxide deposits (*ibid*). The Fe-isotope composition in the sample from the bottom part of the oxide growth, O-12 ( $\delta^{56}\text{Fe} = -0.81\text{‰}$ ) was comparable to other hydrothermal oxides (Bullen et al., 2001; Welch et al., 2003; Moeller et al., 2014); but the exceptionally light isotopic composition of dark surface layer, B-12 ( $\delta^{56}\text{Fe} = -3.01 \pm 0.01 \text{‰}$ ) was lighter than any previous records. Within an individual deposit, such a variation in Fe isotopic compositions indicates diverse modes of oxide precipitation responsible for developing these two layers.

Oxidative precipitation of hydrothermal ferromanganese oxide usually follows a two-step mechanism, which includes initial oxidation of dissolved  $\text{Fe(II)}_{\text{aq}}$  into intermediate  $\text{Fe(III)}_{\text{aq}}$ , followed by precipitation of Fe-oxyhydroxide (Bullen et al., 2001; Welch et al., 2003; Beard and Johnson, 2004). Thus, Fe-isotopic compositions of such oxide deposits are controlled by the isotopic fractionations due to  $\text{Fe(II)}_{\text{aq}}\text{-Fe(III)}_{\text{aq}}$  equilibration and kinetics of Fe-oxyhydroxide precipitation. Laboratory-based experiments show the  $\text{Fe(II)}_{\text{aq}}\text{-Fe(III)}_{\text{aq}}$  equilibrium produce isotopically heavy Fe(III) ( $\Delta^{56}\text{Fe}_{\text{Fe(III)-Fe(II)}} > +3.00\text{‰}$ ), while subsequent rapid precipitation of Fe-oxide is responsible for a fractionation to lighter isotopic compositions ( $\Delta^{56}\text{Fe}_{\text{Fe(III)oxide-Fe(III)aq}} = -2.00\text{‰}$ ). Overall there is a +1‰ fractionation in the transformation from  $\text{Fe(II)}_{\text{aq}}$  to  $\text{Fe(III)}_{\text{oxide}}$  (Beard and Johnson, 2004). Under various experimental conditions, the kinetic fractionation associated with the transformation of  $\text{Fe(III)}_{\text{aq}}$  to  $\text{Fe(III)}_{\text{oxide}}$  is reported to vary between 0.03 to 1.67‰ (see Skulan et al., 2002; Clayton et al., 2005; Balci et al., 2006). This kinetic isotope fractionation is dependent on (i) the temperature, (ii) the nature of the precipitating phase (e.g., ferrihydrite, hematite, etc.) (Beard and Johnson, 2004) and (iii) concentration of Fe in the solution, anion ligands, precipitation rate (Balci et al., 2006). In a natural system, these values may differ due to several factors. However, the measured lighter Fe-isotope compositions in both oxide layers indicate initial aqueous phase  $\text{Fe(III)}_{\text{aq}}\text{-Fe(II)}_{\text{aq}}$  equilibrium fractionation should have resulted in  $\delta^{56}\text{Fe}$  of  $\text{Fe(III)}_{\text{aq}}$  to be close to 0 to 1‰ considering a fractionation associated with the transfer of  $\text{Fe(III)}_{\text{aq}}$  to  $\text{Fe(III)}_{\text{oxide}}$  to be between -1 and -2‰. It is pertinent to mention here that the  $\delta^{56}\text{Fe}$  of  $\text{Fe(III)}_{\text{aq}}$  of deep seawater varies between +0.2 to

+0.8‰(Conway and John, 2014). A large range in  $\delta^{56}\text{Fe}$  values (−1.8 to 1.6‰) was observed in low-temperature hydrothermal plumes (Moeller et al., 2014; Rouxel et al., 2018). The higher  $\delta^{56}\text{Fe}$  values are explained by partial oxidation of Fe in vent fluids under the influence of microbes. In comparison, the lower values are thought to reflect the low-temperature hydrothermal fluids due to prior precipitation of heavy Fe oxides leading to  $^{54}\text{Fe}$  enrichment in the fluid. Although the concentration of iron in deep seawater may be very low 0.2 to 0.4 mol kg<sup>-1</sup> (Conway and John, 2014), the hydrothermally generated Fe(III) would mix with the ambient Fe, and hence the Fe(III)<sub>aq</sub> near the KTJ might have slightly positive  $\delta^{56}\text{Fe}$  values. It is suggested here that rapid precipitation of such Fe(III)<sub>aq</sub> to Fe(III)<sub>oxide</sub> at the KTJ has resulted in the  $^{56}\text{Fe}$  depleted Fe isotope compositions of the oxides near the hydrothermal mound.

The SEM images showed abundant fossil bacterial filaments /networks encrusted with metallic oxides in the O-12 sample (Figs. 5a, b, c). Studies showed that other than abiotic oxidation, hydrothermal fluid precipitation can also be influenced by various microbial processes in the redox cycle of iron (Alt, 1988; Boyd and Scott, 2001; Emerson and Moyer, 2002; Edwards et al., 2011) and such bacterial oxidation can result in precipitation of  $^{56}\text{Fe}$ -rich hydrous Fe-oxide (Croal et al., 2004). The fossilized micro-filaments in the sample O-12 that look very similar to those reported in other low-temperature hydrothermal oxides (e.g., Fortin et al., 1998; Boyd and Scott, 2001; Reysenbach and Cady, 2001; Emerson and Moyer, 2002; Sun et al., 2012) confirm the involvement of Fe-oxidizing bacteria in oxide precipitation. In contrast, the  $^{56}\text{Fe}$ -depleted black colored sample B-12 layer ( $\delta^{56}\text{Fe}=-3.00\text{‰}$ ) at the top of this oxide layer show botryoidal (Figs. 5d and 5e) or rosette-shaped (Fig. 5f) birnessite, and no remnants of microbial communities were found. It is suggested here that after emanation of fluid through fissure openings, the significant fraction of dissolved Fe(II)<sub>aq</sub> undergoes microbial oxidation and precipitation, leaving isotopically lighter-Fe in the residual fluid. Later in the water column, Mn-oxide colloids formed and absorbed lighter Fe-isotopes and precipitate as the B-12 layer on the top of O-12. A similar mechanism for the genesis of hydrothermal oxide has been described by Zeng et al. (2012) in the PACMANUS field. Alternatively, the particles from the hydrothermal plume in the water column may also contribute to the depleted  $^{56}\text{Fe}$  in the B-12 layer, as reported by Severmann et al. (2004) in the Rainbow field.

## 7. Conclusions

In the present study, Fe and S-isotopic compositions were estimated in three types of hydrothermal deposits from an inactive mound at northern Lau basin, and we addressed the following critical aspects of the formation mechanism of these deposits.

(1) The results indicate that the seawater circulation through the hydrothermal reaction zone played a significant role in forming these hydrothermal deposits in a marginal basin. Thus, subduction-induced hydrothermal reactions mediated by higher seawater-rock ratio contribute a considerable fraction of sulfate sulfur and influence metallic sulfide precipitation. The Fe and S isotopic compositions of these back-arc sulfide deposits are mainly influenced by redox processes, zone refinement, and thermal sulfate reduction.

(2) The highly variable Fe and S-isotope compositions of different deposits point to a common hydrothermal source, but their mode of formation is distinct in each deposit type. Similarly, the variable isotopic compositions at different parts or mineral zones within individual deposits also originate due to temporal changes of fluid composition and formation process during the growth of these deposits.

(3) Both Fe and S-isotope ratios in sulfides suggest rapid precipitation rates causing kinetically controlled isotopic fractionation with a limited role for isotopic equilibrium exchange between sulfide and fluid phase. The effects of Fe-isotopic disequilibrium are also prominent in the ferromanganese oxide deposits in which both abiotic and biotic oxidation played a crucial role.

### **Acknowledgments**

We are thankful to the Directors, CSIR-National Institute of Oceanography, Goa, and CSIR-National Geophysical Research Institute, Hyderabad, for their encouragements. This work is part of the GEOSINKS project funded by the Council of Scientific and Industrial Research, India. ALP is highly grateful to Prof. Alexander. P. Lisitsyn for inviting him to participate in the R/V *Akademik Mstislav Keldysh* cruise and providing the samples to undertake scientific investigations. Thanks to V.D. Khedekar for SEM-EDS analyses. BS acknowledges CSIR Raman Research Fellowship and Drs. Andrey Bekker and Boswell Wing for multiple sulfur isotope analysis. Thanks to Dr. Tim Conway, Dr. Torben Stichel, and an anonymous reviewer for their constructive comments on the manuscript.

## References

- Albarede, F., Beard, B.L., 2004. Analytical methods for non-traditional isotopes, in: Johnson, C.M., Beard, B.L., Albarede, F., (Eds.), *Geochemistry of Non-transitional Stable Isotopes*, Rev. Mineral. Geochem., vol. 55, Mineralogical Society of America, Washington, USA. pp. 113–152.
- Alt, J.C., 1988. Hydrothermal oxide and nontronite deposits on seamounts in the eastern Pacific. *Mar. Geol.* 81, 227–239.
- Balci, N., Bullen, T.D., Witte-Lien, K., Shanks, W.C., Motelica, M., Mandernack, K.W., 2006. Iron isotope fractionation during microbially stimulated Fe(II) oxidation and Fe(III) precipitation. *Geochim. Cosmochim. Acta* 70, 622–639.
- Beard, B.L., Johnson, C.M., von Damm K.L., Poulson, R., 2003. Iron isotope constraints on Fe cycling and mass balanced in oxygenated Earth. *Geology* 31, 629–632.
- Beard, B.L., Johnson C.M., 2004. Fe isotope variations in the modern and ancient earth and other planetary bodies. *Rev. Mineral. Geochem.* 55, 319–357.
- Bennett, S.A., Achterberg, E.P., Connelly, D.P., Statham, P.J., Fones, G.R., German, C.R., 2008. The distribution and stabilisation of dissolved Fe in deep-sea hydrothermal plumes. *Earth Planet. Sci. Lett.* 270, 157–167.
- Bennett, S.A., Rouxel, O., Schmidt, K., Garbe-Schönberg, D., Statham, P.J., German, C.R., 2009. Iron isotope fractionation in a buoyant hydrothermal plume, 5°S Mid-Atlantic Ridge. *Geochim. Cosmochim. Acta* 73, 5619–5634.
- Blanchard, M., Poitrasson, F., Meheut, M., Lazzeri, M., Mauri, F., Balan, E., 2009. Iron isotope fractionation between pyrite (FeS<sub>2</sub>), hematite (Fe<sub>2</sub>O<sub>3</sub>) and siderite (FeCO<sub>3</sub>): a first-principles density functional theory study. *Geochim. Cosmochim. Acta* 73, 6565–6578.
- Bluth, G. J., Ohmoto, H., 1988. Sulfide-sulfate chimneys on the East Pacific Rise, 11° and 13°N latitudes. Part II: Sulfur isotopes. *Can. Mineral.* 26, 505–515.
- Boyd, T.D., Scott S.D., 2001. Microbial and hydrothermal aspects of ferric oxyhydroxides and ferrosic hydroxides: the example of Franklin Seamount, Western Woodlark Basin, Papua New Guinea. *Geochem. Trans.* 2, <https://doi.org/10.1186/1467-4866-2-45>.
- Boyle, E.A., Bergquist, B.A., Kayser, R.A., Mahowald, N., 2005. Iron, manganese, lead at Hawaii Ocean Time-series station ALOHA: Temporal variability and an intermediate water hydrothermal plume. *Geochim Cosmochim Acta* 69, 933–952.
- Bullen, T.D., White, A.F., Childs, C.D., Vivit, D.V., Schulz, M.S., 2001. Demonstration of significant abiotic iron isotope fractionation in nature. *Geology* 29, 699–702.
- Butler, I.B., Archer, C., Vance, D., Oldroyd, A., Rickard, D., 2005. Fe isotope fractionation on FeS formation in ambient aqueous solution. *Earth Planet. Sci. Lett.* 236, 430–442.
- Canfield, D.E., Raiswell, R., Westrich, J.T., Reaves, C.M., Berner, R.A., 1986. The use of chromium reduction in the analysis of reduced inorganic sulfur in sediments and shales. *Chem. Geol.* 54, 149–155.



- Carazzo, G., Jellinek, A.M., Turchyn, A.V., 2013. The remarkable longevity of submarine plumes: Implications for the hydrothermal input of iron to the deep-ocean. *Earth Planet. Sci. Lett.* 382, 66–76.
- Chiba, H., Uchiyama, N., Teagle, D.A.H., 1998. Stable isotope study of anhydrite and sulfide minerals at TAG hydrothermal mound, Mid-Atlantic Ridge, 26°N, in: Herzig, P.M., Humphris, S.E., Miller, D.J., Zierenberg, R.A. (Eds.), *Proceedings of the Ocean Drilling Program, Scientific Results*, vol. 158, pp. 85–90.
- Chu, N.-C., Johnson, C.M., Beard, B.L., German, C.R., Nesbitt, R.W., Frank, M., 2006. Evidence for hydrothermal venting in Fe isotope compositions of the deep Pacific Ocean through time. *Earth Planet. Sci. Lett.* 245, 202–217.
- Clayton, R.E., Hudson-Edwards, K.A., Malinovsky, D., Andersson, P., 2005. Fe isotope fractionation during the precipitation of ferrihydrite and transformation of ferrihydrite to goethite. *Mineral. Mag.* 69, 667–676.
- Conway, T.M., John, S.G., 2014. Quantification of dissolved iron sources into the North Atlantic Ocean. *Nature* 511, 212–215.
- Conway, T.M., John, S.G., Lacan, F., 2016. Intercomparison of dissolved iron isotope profiles from reoccupation of three GEOTRACES stations in the Atlantic Ocean. *Mar. Chem.*, 183, 50–61.
- Coplen, T.B., Krouse, H.R., 1998. Sulphur isotope data consistency improved. *Nature* 392, 32.
- Croal, L.R., Johnson, C.M., Beard, B.L., Newman, D.K., 2004. Iron isotope fractionation by Fe(II)-oxidizing photoautotrophic bacteria. *Geochim. Cosmochim. Acta* 68, 1227–1242.
- Dauphas, N., Rouxel, O., 2006. Mass spectrometry and natural variations of iron isotopes. *Mass Spec. Rev.* 25, 831–832.
- Dauphas, N., John, S.G., Rouxel, O., 2017. Iron isotope systematics. *Rev. Min. Geochem.* 82, 415–510.
- Dril, S.I., Kuzmin, M.I., Tsipukova, S.S., Zonenshain, L.P., 1997. Geochemistry of basalts from western Woodlark, Lau and Manus basins: Implication for their petrogenesis and source rock compositions. *Mar. Geol.* 142, 57–83.
- Duckworth, R.C., Knott, R., Fallick, A.E., Rickard, D., Murton, B.J., Dover, C.V., 1995. Mineralogy and sulphur isotope geochemistry of the Broken Spur sulfides, 29°N, Mid-Atlantic Ridge, in: Parson, L.M., Walker, C.L., Dixon, D.R. (Eds.), *Hydrothermal Vents and Processes*, vol. 87, pp. 175–189.
- Edwards, K.J., Glazer, B.T., Rouxel, O.J., Bach, W., Emerson, D., Davis, R.E., Toner, B.M., Chan, C.S., Tebo, B.M., Staudigel, H., Moyer, C.L., 2011. Ultra-diffuse hydrothermal venting supports Fe-oxidizing bacteria and massive uranium deposition at 5000m off Hawaii. *The ISME Journal* 5, 1748–1758.
- Elderfield, H., Schulz, A., 1996. Mid-ocean ridge hydrothermal fluxes and the chemical composition of the ocean. *Ann. Rev. Earth Planet. Sci.* 24, 191–224.

- Emerson, D., Moyer, C.L., 2002. Neutrophilic Fe-Oxidizing bacteria are abundant at the Loihi Seamount hydrothermal vents and play a major role in Fe-oxide deposition. *Appl. Env. Microbiology* 68, 3085–3093.
- Falloon, T.J., Malahoff, A., Zonenshain, L.P., Bogbanov, Y., 1992. Petrology and geochemistry of back-arc basin basalt from Lau spreading ridges at 15°, 18° and 19°S. *Mineral. Petrol.* 47, 1–35.
- Fitzsimmons, J.N., Boyle, E.A., Jenkins, W.J., 2014. Distal transport of dissolved hydrothermal iron in the deep South Pacific Ocean. *Proc. Natl. Acad. Sci.* 111, 16654–16661.
- Fitzsimmons, J.N., John, S.G., Marsay, C.M., Hoffman, C.L., Nicholas, S.L., Toner, B.M., German, C.R., Sherrell, R.M., 2017. Iron persistence in a distal hydrothermal plume supported by dissolved-particulate exchange. *Nat. Geosci.* 10, 195–201.
- Fouquet, Y., Von Stackelberg, U., Charlou, J.L., Donval, J.P., Erzinger, J., Foucher, J.P., Herzig, P., Muhe, R., Soakai, S., Wiedicke, M., Whitechurch, H., 1991. Hydrothermal activity and metallogenesis in the Lau back arc basin. *Nature* 349, 778–781.
- Fouquet, Y., Von Stackelberg, U., Charlou, J.L., Erzinger, J., Herzig, P.M., Mühe, R., Wiedicke, M., 1993. Metallogenesis in back-arc environments: the Lau Basin example. *Econ. Geol.* 88, 2154–2181.
- Fortin, D., Ferris, F.G., Scott, S.D., 1998. Formation of Fe-silicates and Fe-oxides on bacterial surfaces in samples collected near hydrothermal vents on the Southern Explorer Ridge in the northeast Pacific Ocean. *Am. Mineral.* 83, 1399–1408.
- Gemmell, J.B., Binns, R.A., Parr, J.M., 1996. Comparison of sulfur isotope values between modern back-arc and mid-ocean ridge seafloor hydrothermal systems. *Eos Trans.* 77, 117.
- Gemmell, J.B., Sharpe, R., 1998. Detailed Sulfur-isotope investigation of the hydrothermal mound and stockwork zone, 26°N, Mid-Atlantic ridge, in: Herzig, P.M., Humphris, S.E., Miller, D.J., Zierenberg, R.A. (Eds.), *Proceedings of ODP Science Results*, vol. 158, pp. 71–84.
- German, C.R., Seyfried, W.E.J., 2014. Hydrothermal processes, in: Holland, H.D., Turekian, K.K. (Eds.), *Treatise on Geochemistry* (2nd Edition), vol. 8, pp. 191–233.
- German, C.R., Von Damm, K.L., 2003. Hydrothermal processes, in: Holland, H.D., Turekian, K.K. (Eds.), *The Oceans and Marine Geochemistry, Treatise on Geochemistry*, vol. 6, pp. 181–222.
- German, C.R., Elderfield, H., 1990. Application of the Ce anomaly as a paleoredox indicator: the ground rules. *Paleocean.* 5, 823–833.
- Glasby, G. P., Notsu, K., 2003. Submarine hydrothermal mineralization in the Okinawa Trough, SW of Japan: an overview. *Ore Geol. Rev.* 23, 299–339.
- Guilbaud, R., Butler, I.B., Ellam, R.M., 2011. Abiotic pyrite formation produces a large Fe isotope fractionation. *Science* 332, 1548–1551.
- Hawkins, J.W., 1995. The Geology of the Lau Basin, in: Taylor, B. (Ed.), *Backarc Basins - Tectonics and Magmatism*. Plenum Press, New York and London, pp. 63–138.

- Herzig, P.M., Hannington, M.D., Arribas, A., 1998. Sulfur isotopic composition of hydrothermal precipitates from the Lau back-arc: implications for magmatic contributions to seafloor hydrothermal systems. *Mineral. Deposit.*33, 226–237.
- Horner, T.J., Williams, H.M., Hein, J.R., Saito, M.A., Burton, K.W., Halliday, A.N., Nielsen, S.G., 2015. Persistence of deeply sourced iron in the Pacific Ocean. *Proc. Natl. Acad. Sci.*112, 1292–1297.
- Humphris, S.E., Herzig, P.M., Miller, D.J., Alt, J.C., Becker, K., Brown, D., Bruegmann, G., Chiba, H., Fouquet, Y., Gemmill, J.B., Guerin, G., Hannington, M.D., Holm, N.G., Honnorez, J.J., Iturrino, G.J., Knott, R., Ludwig, R., Nakamura, K., Petersen, S., Reysenbach, A.L., Rona, P.A., Smith, S., Sturz, A.A., Tivey, M.K., Zhao, X., 1995. The internal structure of an active seafloor massive sulphide deposit. *Nature*377, 713–716.
- Janecky, D.R., Shanks, W.C. III., 1988. Computational modeling of chemical and isotope reaction processes in seafloor hydrothermal systems: chimneys, massive sulfides, and subjacent alteration zones. *Can. Mineral.*,26, 805–825.
- Johnson, C.M., Beard, B.L., Roden, E.E., Newman, D.K., Nealson, K.H., 2004. Isotopic constraints on biogeochemical cycling of Fe, in: Johnson, C.M., Beard B.L., Albarede, F. (Eds.), *Geochemistry of non-traditional stable isotopes*, vol. 55 Mineralogical Society of America, Washington, USA. pp. 359–408.
- Lecuyer, C., Dubois, M., Marignac, C., Gruau, G., Fouquet, Y., Ramboz, C., 1999. Phase separation and fluid mixing in subseafloor back arc hydrothermal systems: A microthermometric and oxygen isotope study of fluid inclusions in the barite-sulfide chimneys of the Lau Basin. *J. Geophys. Res.*104 (B3), 17911–17927.
- Li, X., Wang, J., Chu, F., Wang, H., Li, Z., Yu, X., Bi, D., He, Y., 2018. Variability of Fe isotope compositions of hydrothermal sulfides and oxidation products at mid-ocean ridges. *J. Mar. Syst.*180, 191–196.
- Lisitsyn, A.P., Malahoff, A.R., Bogdanov, Y.A., Soakai, S., Zonenshayn, L.P., Gurchich, Y.G., Murav'yev, K.G., Ivanov, G.V., 1992. Hydrothermal formations in the northern part of the Lau Basin, Pacific Ocean. *Int. Geol. Rev.*34(8), 828–847.
- Lisitsyn, A.P., Crook, K.A.W., Bogdanov, Y.A., Zonenshayn, L.P., Murav'yev, K.G., Tufar, W., Gurchich, Y.G., Gordeyev, V.V., Ivanov, G.V., 1993. A hydrothermal field in the rift zone of the Manus basin, Bismark Sea. *Int. Geol. Rev.*35, 105–126.
- Marèchal, C.N., Telouk, P., Albarède, F., 1999. Precise analysis of copper and zinc isotopic composition by plasma-source mass spectrometry. *Chem. Geol.* 156, 251–273.
- McDermott, J.M., Sylva, S.P., Ono, S., German, C.R., Seewald, J.S. 2020. Abiotic redox reactions in hydrothermal mixing zones: Decreased energy availability for the subsurface biosphere. *Proc. Natl. Acad. Sci.* 117, 20453–20461.
- Moeller, K., Schoenberg, R., Grenne, T., Thorseth, I.H., Kerstin D., Pedersen R.B., 2014. Comparison Iron isotope variations in modern and Ordovician siliceous Fe oxyhydroxide deposits. *Geochim. Cosmochim. Acta*126, 422–440.

- Ono, S., Wing, B.A., Johnston, D., Farquhar, J., Rumble, D., 2006. Mass dependent fractionation of quadruple sulfur isotope system as a new tracer of sulfur biogeochemical cycles. *Geochim. Cosmochim. Acta* 70, 2238–2252.
- Ono, S., Shanks, W.C., Rouxel, O.J., Rumble, D., 2007. Multiple-sulfur isotope constraints on the seawater sulfate contribution in modern seafloor hydrothermal sulfide. *Geochim. Cosmochim. Acta* 71, 1170–1182.
- Paropkari, A.L., Ray, D., Balaram, V., Surya Prakash, L., Mirza, H.I., Satyanarayanan, M., Rao, T.G., Kaisary, S., 2010. Formation of hydrothermal deposits at Kings Triple Junction, northern Lau back-arc basin, SW Pacific: The geochemical perspectives. *J. Asian Earth Sci.* 38, 121–130.
- Parsons, L.M., Tiffin, D.L., 1993. Northern Lau basin: Backarc extension at the leading edge of the Indo-Australian plate. *Geo-Mar. Lett.* 13, 107–115.
- Polyakov, V.B., Clayton, R.N., Horita, J., Mineev, S.D., 2007. Equilibrium iron isotope fractionation factors of minerals: reevaluation from the data of nuclear inelastic resonant X-ray scattering and Mossbauer spectroscopy. *Geochim. Cosmochim. Acta* 71, 3833–3846.
- Polyakov, V.B., Soultanov, D.M., 2011. New data on equilibrium isotope fractionation among sulfides: Constraints on mechanisms of sulfide formation in hydrothermal and igneous systems. *Geochim. Cosmochim. Acta* 75, 1957–1974.
- Ray, D., Kota, D., Das, P., Surya Prakash L., Khedekar, V.D., Paropkari, A.L., Mudholkar, A.V., 2014. Microtexture and distribution of minerals in hydrothermal barite-silica chimney from the Franklin Seamount, SW Pacific: Constraints on mode of formation. *Geol. Sin. Acta* 88, 213–225.
- Ray, D., Banerjee, R., Mazumdar, A., Paropkari, A.L., Mukhopadhyay, S., Balakrishnan, S., 2018. Mineralogical and geochemical variation in hydrothermal sulfides from Vienna Woods field, Manus Basin, Papua New Guinea: constraints on their evolution. *Ocean. Sin. Acta* 37, 22–33.
- Rees, C.E., Jenkins, W.J., Monster, J., 1978. The sulphur isotopic composition of ocean water sulphate. *Geochim. Cosmochim. Acta* 42, 377–381.
- Resing, J.A., Sedwick, P.N., German, C.R., Jenkins, W.J., Moffett J.W., Sohst B.M., Tagliabue, A., 2015. Basin-scale transport of hydrothermal dissolved metals across the South Pacific Ocean. *Nature* 523, 200–203.
- Rouxel, O., Dobbek, N., Ludden, J., Fouquet, Y., 2003. Iron isotope fractionation during oceanic crust alteration (Site ODP 801). *Chem. Geol.* 202, 155–182.
- Rouxel, O., Fouquet, Y., Ludden J.N., 2004. Subsurface processes at the Lucky Strike hydrothermal field, Mid Atlantic Ridge: Evidences from sulfur, selenium, and iron isotopes. *Geochim. Cosmochim. Acta* 68, 2295–2311.
- Rouxel, O., Shanks, W.C., Bach, W., Edwards, K.J., 2008. Integrated Fe and S-isotope study of seafloor hydrothermal vents at East pacific Rise 9-10°N. *Chem. Geol.* 252, 214–227.
- Rouxel, O., Toner, B., Manganini, S., German, C.R., 2016. Geochemistry and iron isotope systematics of hydrothermal plume fall-out at EPR 9°50'N. *Chem. Geol.* 441, 212–234.

- Rouxel, O., Toner, B., Germain, Y., Glazer, B., 2018. Geochemical and iron isotopic insights into hydrothermal iron oxyhydroxide deposit formation at Loihi Seamount. *Geochim. Cosmochim. Acta* 220, 449–482.
- Saito, M.A., Noble, A.E., Tagliabue, A., Goepfert, T.J., Lamborg, C.H., Jenkins, W.J., 2013. Slow-spreading submarine ridges in the South Atlantic as a significant oceanic iron source. *Nat. Geosci.* 6, 775–779.
- Severmann, S., Johnson, C.M., Beard, B.L., German, C.R., Edmonds, H.N., Chiba, H., Green, D.R.H., 2004. The effect of plume processes on the Fe isotope composition of hydrothermally derived Fe in the deep ocean as inferred from the Rainbow vent sites, Mid-Atlantic Ridge, 36°14'N. *Earth Planet. Sci. Lett.* 225, 63–76.
- Shanks, W.C., Seyfried W.E., 1987. Stable isotope studies of vent fluids and chimney minerals, Southern Juan de Fuca Ridge: Sodium metasomatism and seawater sulfate reduction. *J. Geophys. Res.* 92, 11387–11399.
- Shanks, W.C., 2001. Stable isotopes in seafloor hydrothermal systems: vent fluids, hydrothermal deposits, hydrothermal alteration, and microbial processes, in: Valley, J.W., Cole, D.R. (Eds.), *Stable Isotope Geochemistry: Rev. Mineral. Geochem.*, vol. 43, pp. 469–525.
- Sharma, M., Polizzotto, M., Anbar, A.D., 2001. Iron isotopes in hot spring along the Juan de Fuca Ridge. *Earth Planet. Sci. Lett.* 194, 39–51.
- Skulan, J.L., Beard, B.L., Johnson, C.M., 2002. Kinetic and equilibrium Fe isotope fractionation between aqueous Fe(III) and hematite. *Geochim. Cosmochim. Acta* 66, 2995–3015.
- Sreenivas, B., Ray, D., Paropkari, A.L., Mazumdar, A., Vijaya Gopal, B., Surya Prakash, L., Balu, G., and Bhaskar Rao, Y.J., 2011. Fe and S isotope compositions of hydrothermal sulfides from the northern Lau Basin. *Mineral. Mag.* 75(3), p. 1926.
- Styrt, M.M., Brackmann, A.J., Holland, H.D., Clark, B.C., Pisutha-Arnond, V., Eldridge, C.S., Ohmoto, H., 1981. The mineralogy and the isotopic composition of sulfur in hydrothermal sulfide/sulfate deposits on the East Pacific Rise, 21°N latitude. *Earth Planet. Sci. Lett.* 53, 382–390.
- Sun, Z., Zhou, H., Glasby, G.P., Yang, Q., Yin, X., Li, J., Chen, Z., 2012. Formation of Fe–Mn–Si oxide and nontronite deposits in hydrothermal fields on the Valu Fa Ridge, Lau Basin. *J. Asian Earth Sci.* 43, 64–76.
- Swanner, E.D., Bayer, T., Wu, W., Hao, L., Obst, M., Sundman, A., Byrne, J.M., Michel, F.M., Kleinhanns, I.C., Kappler, A., Schoenberg, R. 2017. Iron isotope fractionation during Fe(II) oxidation mediated by the oxygen-producing marine cyanobacterium *synechococcus* PCC 7002. *Env. Sci. Tech.* 51, 4897–4906.
- Syverson, D.D., Borrok, D.M., Seyfried, W.E. 2013. Experimental determination of equilibrium Fe isotopic fractionation between pyrite and dissolved Fe under hydrothermal conditions. *Geochim. Cosmochim. Acta* 122, 170–183.
- Tagliabue, A., Bopp, L., Dutay J.C., Bowie, A.R., Chever, F., Jean-Baptiste, P., Bucciarelli, E., Lannuzel, D., Remenyi, T., Sarthou G., Aumont, O., 2010. Hydrothermal contribution to the oceanic dissolved iron inventory. *Nat. Geosci.* 3, 252–256.

- Tagliabue, A., Aumont, O., Bopp, L., 2014. The impact of different external sources of iron on the global carbon cycle. *Geophys. Res. Lett.*41,920–926
- Tivey, M.K., Humphris, S.E., Thompson, G.,Hannington, M.D., Rona, P.A.,1995. Deducing patterns of fluid flow and mixing within the TAG active hydrothermal mound using mineralogical and geochemical data. *J.Geophys. Res.*100(B3), 12527–12555.
- Toner, B.M., Fakra, S.C., Manganini, S.J., Santelli, C.M., Marcus, M.A., Moffett, J., Rouxel, O., German, C.R.,Edwards, K.J., 2009. Preservation of iron(II) by carbon-rich matrices in a hydrothermal plume. *Nat. Geosci.*2,197–201.
- Wagner, T., Cook, N.J.,1998. Sphalerite remobilization during multistage hydrothermal mineralization events-examples from siderite-Pb-Zn-Cu-Sb veins, Rheinisches Schiefergebirge, Germany. *Mineral. and Petrol.*63, 223–241.
- Welch, S.A., Beard, B.L., Johnson, C.M., Braterman, P.S.,2003. Kinetic and equilibrium Fe isotope fractionation between aqueous Fe(II) and Fe(III). *Geochim. Cosmochim. Acta*67, 4231–4250.
- Woodruff, L.G., Shanks, W.C.,1988. Sulfur isotope study of chimney minerals and vent fluids from 21°N, East Pacific Rise: Hydrothermal sulfur sources and disequilibrium sulfate reduction. *J.Geophys. Res.* 93(B5), 4562–4572.
- Wu, J., Wells, M.L., Rember, R.,2011. Dissolved iron anomaly in the deep tropical- subtropical Pacific: evidence for long-range transport of hydrothermal iron. *Geochim. Cosmochim. Acta*75, 460–468.
- Zeng, Z., Ouyang, H., Yin, X., Chen, S., Wang, X., Wu, L.,2012. Formation of Fe–Si–Mn oxyhydroxides at the PACMANUS hydrothermal field, Eastern Manus Basin: Mineralogical and geochemical evidence. *J. Asian Earth Sci.*60, 130–146.
- Zeng, Z., Ma, Y., Chen, S., Selby, D., Wang, X., Yin, X., 2017. Sulfur and lead isotopic compositions of massive sulfides from deep-sea hydrothermal systems: implications for ore genesis and fluid circulation. *Ore Geol.Rev.*87, 155–171.

## Figure captions:

**Figure 1.** (a) Bathymetric map of the Lau Basin in the Southwest Pacific Ocean. The square shows the location of the Kings Triple Junction (KTJ) in the northern Lau basin (modified after Paropkari et al., 2010). (b) Detailed seafloor features around the KTJ. The diving site of submersible M2226 shows the location of the extinct hydrothermal field.

**Figure 2.** (a) Schematic diagram of the extinct hydrothermal mound near KTJ, showing its approximate dimension. (b) Diagram of the peripheral chimney, M2226-6. (c) Six sub-sections (S1 to S6) of the lateral section, M2226-6/12 of the hydrothermal chimney. (d) Four layers (L1 to L4) of the vertical section of the pedestal slab, M2226-5, of the main mound. (e) Two layers (B-12 and O-12) of oxide growth, M2226-12, from the "Christmas Tree" field (modified after Paropkari et al., 2010).

**Figure 3.** SEM-EDS results of L4 and L3 layers in pedestal slab. (a) Image of large chalcopyrite crystals in the top L4 layer. (b) EDS pattern of chalcopyrite crystals. (c) Sphalerite crystals in the intermediate dark layer L3 and (d) corresponding EDS pattern.

**Figure 4.** SEM-EDS results of particles from the chimney section, M2226-6/12. (a) Image of euhedral sphalerite crystal in the intermediate section, S4 of the chimney wall, and (b) corresponding EDS plot. (c) Globular colloform silica within sphalerite crystals in the outermost rim of the chimney (section S1). (d) EDS patterns for silica deposits.

**Figure 5.** SEM images of O12 (a-c) and B12 (d-f) layers of ferromanganese oxide, M2226-12. The images of O-12 show fossilized microbial growths with Fe-oxide coatings. B-12 appeared as an orb-like structure, and further magnified images show a crystalline network of typical birnessite.

**Figure 6.** Plots showing the relation between isotope compositions and bulk elemental concentrations in pedestal slab and peripheral chimney. (a)  $\delta^{34}\text{S}$  vs. Zn; (b)  $\delta^{56}\text{Fe}$  vs. Zn; (c)  $\delta^{56}\text{Fe}$  vs. Cu and (d)  $\delta^{56}\text{Fe}$  vs. Fe.

**Figure 7.** Plots of Fe and S-isotope compositions against cerium anomaly in bulk sub-samples of sulfide deposits from pedestal slab and peripheral chimney. A good co-relation between Fe-isotope and Ce-anomaly indicates redox control in Fe-isotope fractionation.

**Table 1:** Mineralogy, major and trace element concentration, and isotopic compositions of sulfur and iron in the sub-samples of pedestal slab, peripheral chimney, and Fe-Mn-oxide growth. The mineralogical and elemental data are from Paropkari et al., 2010.

	Pedestal slab				Peripheral chimney						Oxide growth	
	(M2226-5)				(M2226-6/12)						(M2226-12)	
Sub-samples	L1	L2	L3	L4	S1	S2	S3	S4	S5	S6	B-12	O-12
Major minerals*	Py, Chl, Ba	Py, Chl, Ba	Sph	Py, Chl	Sph	Sph	Sph	Sph	Sph	Sph	Bir	Amp ox
Mn (%)	0.02	0.01	0.03	0.02	0.03	0.06	0.04	0.04	0.03	0.03	32.2	0.09
Fe (%)	8.09	8.6	2.87	12.5	1.73	1.53	4.37	1.18	1.39	1.84	1.33	14.5
Cu (%)	7.39	11.4	4.48	16.4	1.54	1.52	1.08	1.22	1.05	1.1	0.01	0.01
Zn (%)	1.14	2.25	23.9	7.29	32.8	25.6	23.8	34	29.2	28	0.18	0.01
Ni (ppm)	16.6	14.7	17.8	14.5	22.3	16.1	22	19.3	22.2	17.6	87.4	15.6
Co (ppm)	0.49	0.48	0.45	0.45	0.65	0.6	0.72	0.49	0.71	0.5	1.56	3.83
ΣREE (ppm)	16.3	7.39	0.93	5.86	1.12	0.77	0.79	0.91	0.65	0.71	1.66	1.88
Eu <sub>n</sub> /Sm <sub>n</sub>	122	91.2	19.9	82.9	5.49	4.85	2.93	2.26	3.9	4.6	3.34	2.49
Ce-anomaly	0.31	0.37	0.66	0.47	0.97	0.78	0.78	0.74	0.99	0.75	0.36	0.42
δ <sup>34</sup> S <sub>V-CDT</sub> (‰)	9.6	9.8	8.3	8.5	5.5	6.9	7.5	7.9	8.1	8.3	NA	NA
δ <sup>33</sup> S <sub>V-CDT</sub> (‰)			4.55 ±0.004							4.95 ±0.004		
δ <sup>34</sup> S <sub>V-CDT</sub> (‰)			8.84 ±0.004							9.62 ±0.007		
δ <sup>36</sup> S <sub>V-CDT</sub> (‰)			16.66 ±0.09							18.1 ±0.06		
Δ <sup>33</sup> S (‰)			0.014 ±0.007							0.009 ±0.004		
Δ <sup>36</sup> S (‰)			-0.21 ±0.08							-0.22 ±0.06		
δ <sup>56</sup> Fe <sub>IRMM14</sub> (‰) ±SD (1σ)	-1.14 ±0.05	-0.96 ±0.12	-0.33 ±0.02	-1.11 ±0.01	-0.62 ±0.04	-1.38 ±0.11	-1.31 ±0.10	-0.97 ±0.03	-0.99 ±0.07	-1.70 ±0.01	-3.01 ±0.10	-0.81 ±0.02
δ <sup>57</sup> Fe <sub>IRMM14</sub> (‰) ±SD (1σ)	-1.58 ±0.19	-1.43 ±0.12	-0.40 ±0.06	-1.64 ±0.18	-0.99 ±0.11	-1.90 ±0.15	-1.80 ±0.18	-1.29 ±0.07	-1.49 ±0.14	-2.69 ±0.20	-4.59 ±0.14	-1.18 ±0.18

\*Py: Pyrite; Chl: Chalcopyrite; Ba: Barite; Sph: Sphalerite; Bir: Birnessite; Amp ox: Amorphous Fe-oxide.



Figures:

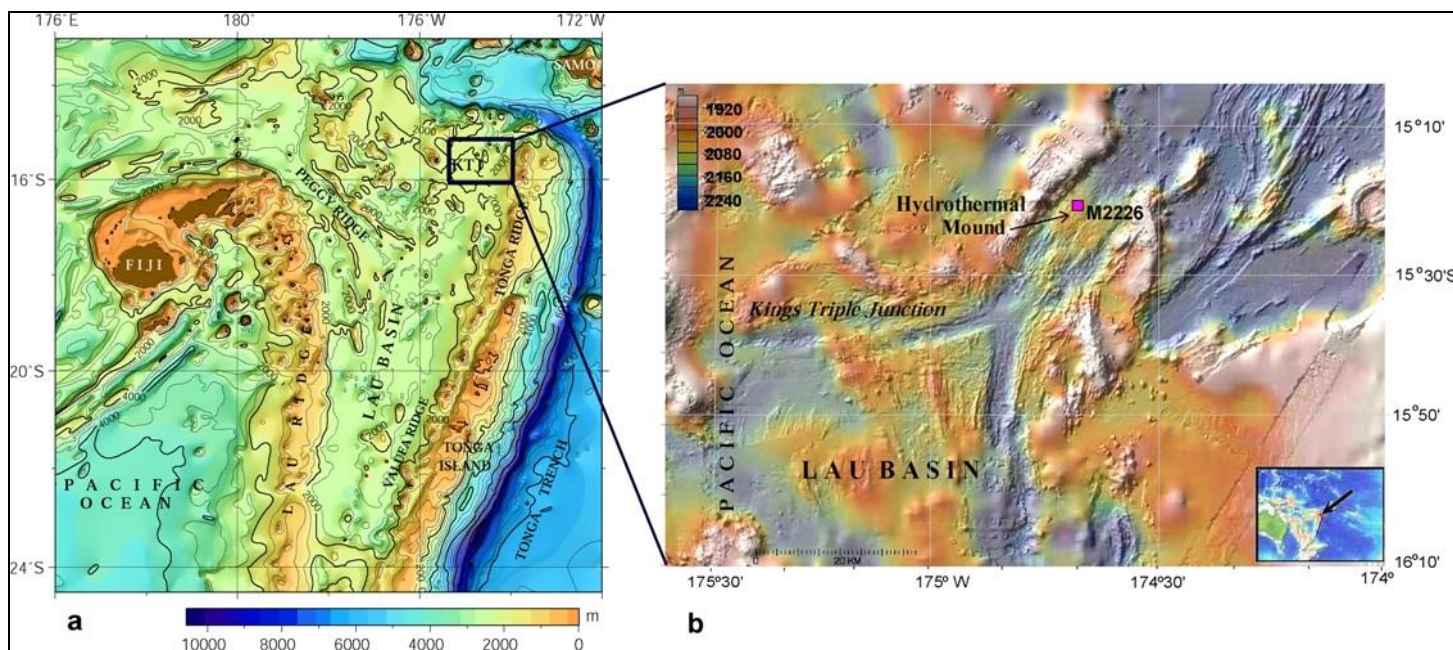


Figure 1.

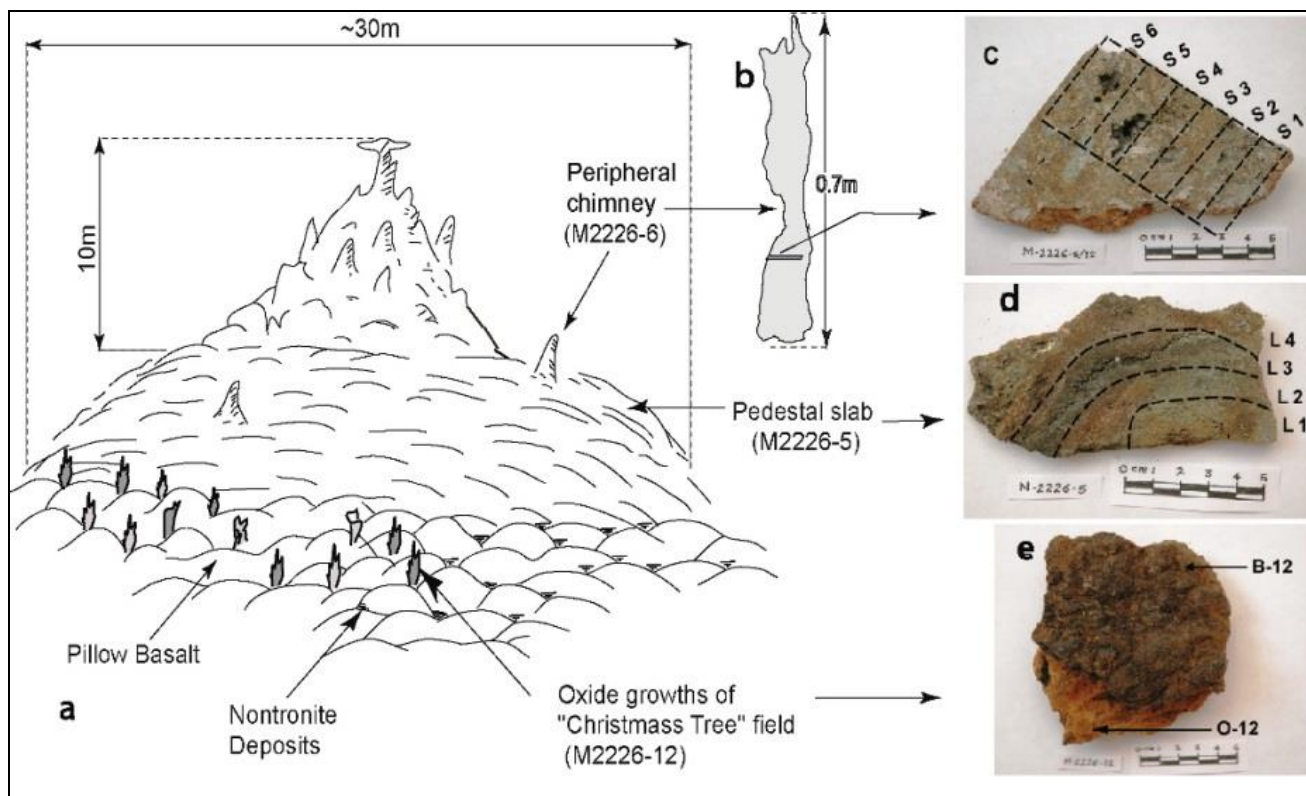
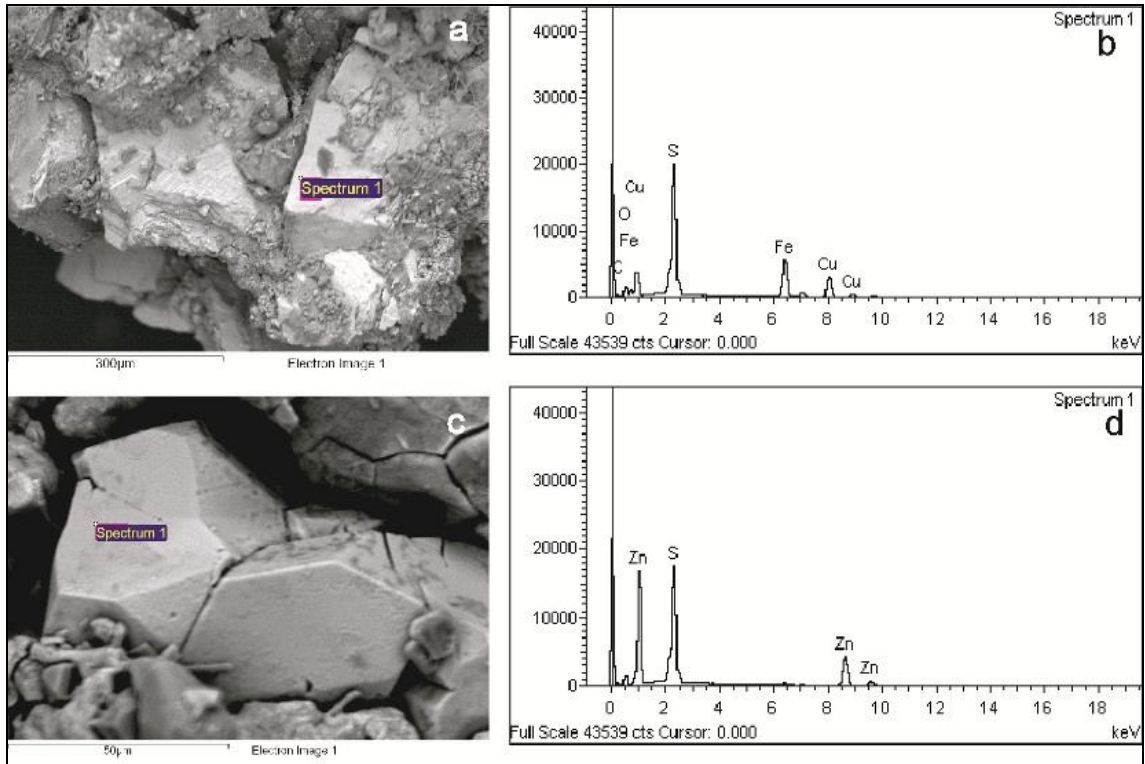
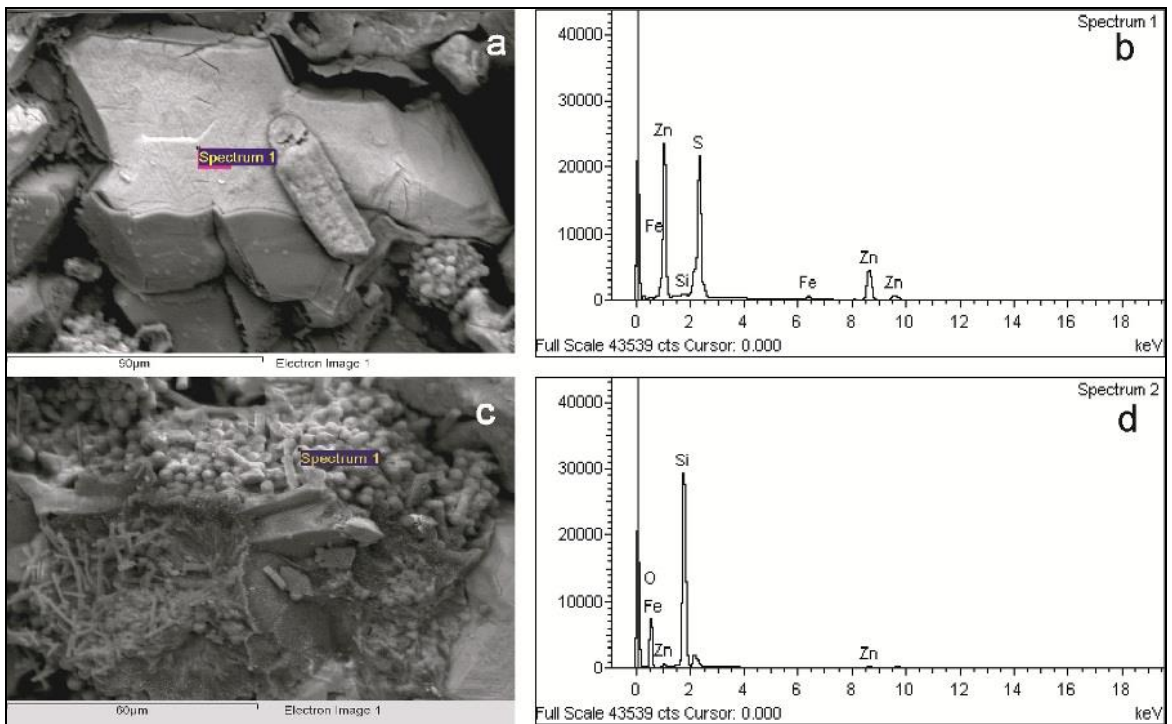


Figure 2.



**Figure 3.**



**Figure 4.**

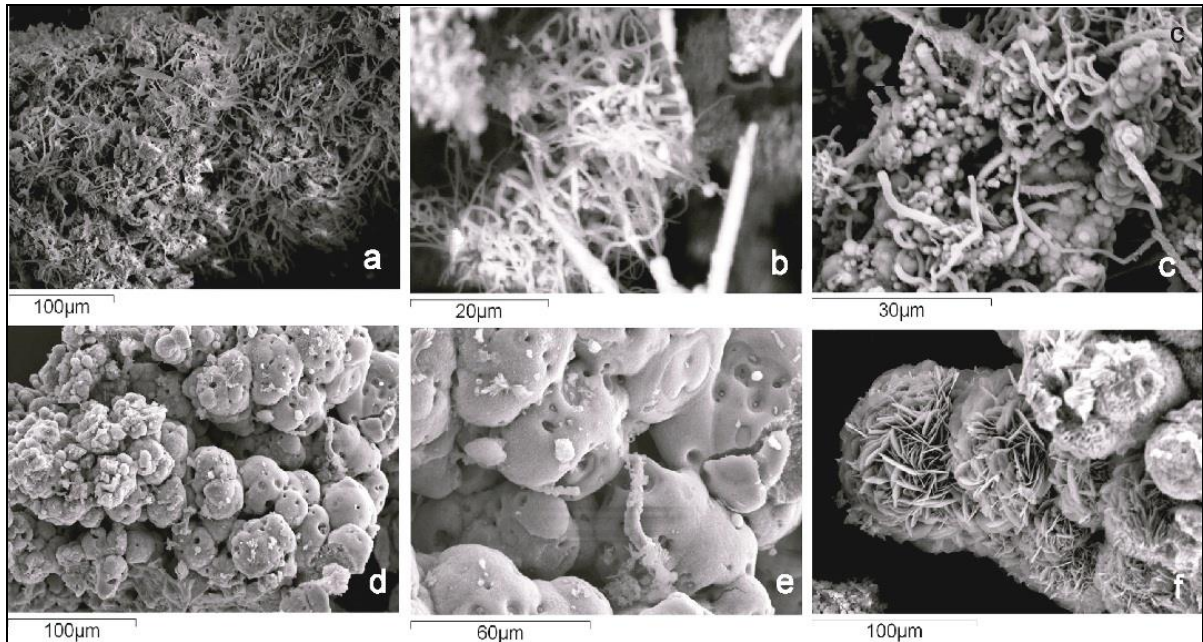


Figure 5.

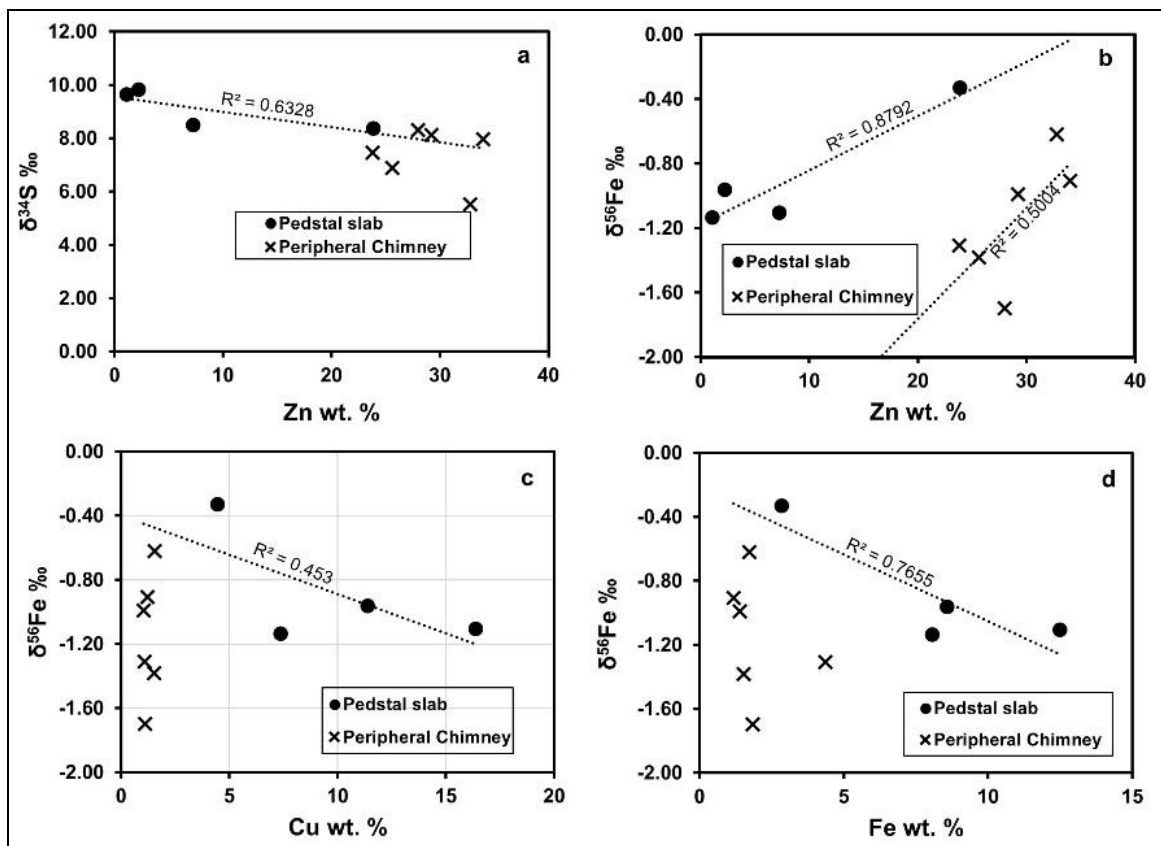


Figure 6.

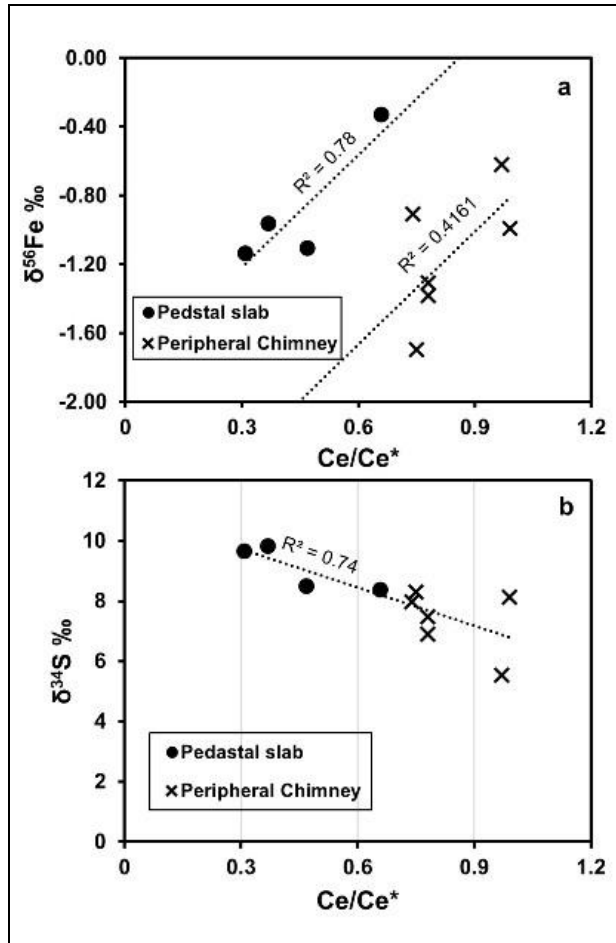


Figure 7.